J Solid State Electrochem (2002) 6: 420–427
DOI 10.1007/s100080100244

ORIGINAL PAPER

Mao-Hui Chen · Guo-Tao Wu · Guang-Ming Zhu
Jin-Kua You · Zu-Geng Lin

Characterization and electrochemical investigation of boron-doped mesocarbon microbead anode materials for lithium ion batteries

Received: 22 March 2001 / Accepted: 16 July 2001 / Published online: 16 October 2001
© Springer-Verlag 2001

Abstract The structure and anodic performance of boron-doped and undoped mesocarbon microbeads (MCMBs) have been comparatively studied and the results obtained by XPS, XRD, SEM, Raman spectroscopy and electrochemical measurements are discussed. It is found that boron doping introduces a depressed d_{002} spacing and the larger amount of ''unorganized carbon'', which induces vacancy formation in the graphite planes and leads to a quite different morphology from that of the undoped material. Electrochemical charge/discharge cycle tests indicated that after boron doping the lithium intercalation was carried through at a somewhat higher potential, being attended by greater irreversible capacity loss.

Keywords Mesocarbon microbeads · Boron doping · Electrochemical properties

Introduction

In recent years, boron-doped carbon materials have been received much attention for their use as host materials for lithium intercalation [1, 2]. It has been established that boron doping can modify the electronic properties of the carbon graphitic network as boron is a neighbor to carbon in the Periodic Table but has one electron less [3]. Experimental and theoretical investigations have pointed out that boron doping is prompting an electron acceptor level, inducing positive holes in the energy band of matrix graphite, and hence the battery performance can be expected to be improved if boron-doped carbon is used in lithium ion batteries as an anode material [4, 5, 6, 7, 8]. In carbonaceous materials, boron atom is a graphitization catalyst, which can alter the host structure of carbon greatly [9]. If the change is concerned with structural factors such as the *a-b* axis crystallite size, stacking fidelity, and defects of the basal planes, significant effects on the anode electrochemical performance with respect to lithium insertion can be proposed [10, 11].

In various soft carbon materials applied in lithium ion batteries, mesocarbon microbeads (MCMBs) are most attractive because of their unique spherical structure and low surface area, which lead to a high packing density and suppression of side reactions with the electrolyte during discharging and charging [12, 13]. In the past decade, MCMBs have received extensive studies on their structure and properties, and finally are used widely in commercial lithium ion batteries [2, 11, 12, 13, 14, 15, 16]. However, most of the research work has been focused on the heat treatment of MCMBs, with little work concerned with the boron-doped MCMBs as anode materials [17, 18]. In the present study, the effect of boron doping on the microstructure characteristics and electrochemical properties of MCMBs will be investigated and discussed in detail.

Experimental

The undoped and boron-doped MCMBs were supplied by Kawasaki Steel (Japan) and used without any pretreatment. The boron-doping process, as described by the manufacturer, was accomplished by mixing the pristine MCMBs with B_2O_3 and then heat treating the resulting material to 2800 °C in argon gas. The boron content was determined to be about 6.9 at% by XPS. The two as-received samples were characterized by instrumental analyses, such as XPS, field-emission SEM, XRD, and Raman scattering to investigate the chemical binding energies of the elements, the samples' morphologies, crystal structures, and the microcosmic chemical environments of the carbon atoms. During the analyses, XPS measurements were carried out using Mg K_α X-ray radiation. Morphology observations were accomplished on a Hitachi S-4100 field-emission SEM instrument under 20 kV acceleration voltage. An X-ray diffractometer (Rigaku Rotaflex D/max-C) with Cu K_α ($\lambda = 0.154056$ nm) radiation and a graphite monochromator was

M.-H. Chen (✉) · G.-T. Wu · G.-M. Zhu · J.-K. You
Z.-G. Lin
State Key Laboratory for Physical Chemistry
of Solid Surfaces and Department of Chemistry,
Xiamen University, Xiamen, Fujian 361005, P.R. China
E-mail: mhchen8@yanan.xmu.edu.cn
Tel.: +86-592-2183905
Fax: +86-592-2183905

used to collect the XRD data. A confocal microprobe Raman system (LabRam I) equipped with a 514.5 nm/5 mW Ar-ion laser excitation source and a charge-coupled device (CCD) multichannel detector was used to record the Raman scattering spectra at room temperature under ambient conditions.

All electrochemical measurements were performed using a three-electrode test cell made of glass. The working electrode was prepared by mixing 95 wt% of the undoped or boron-doped MCMBs with 5 wt% polytetrafluoroethylene (PTFE) as binder. The gum-like mixture obtained was spread to a thin film and pressed onto a nickel mesh (5×5 mm) at 10 MPa, and then dried under vacuum for 24 h at 120 °C. The electrolyte used was 1 M $LiPF_6$ dissolved in a mixed solvent of 50% ethylene carbonate (EC) and 50% dimethyl carbonate (DMC) by volume. Lithium metal was used both as the counter electrode and as the reference electrode. Cell assembly operations were carried out in a glove box filled with argon gas, where water and oxygen concentrations were kept less than 3 ppm. Discharge/charge cycle testing was implemented on an Arbin BT-2043 battery test system in a voltage range from 0.005 to 3.0 V and with a constant discharge/charge rate of 40 mA/g.

Results and discussion

XPS of the materials

The whole XPS patterns of the two samples are comparatively shown in Fig. 1. It can be seen clearly that besides the common C_{1s} and O_{1s} peaks, the boron-doped MCMB has a unique B_{1s} peak at around 186.5–90.5 eV and an additional N_{1s} peak at around 398.0–399.0 eV. The B_{1s} peak is the characteristic peak of the boron-doped sample, but the N_{1s} peak is unexpected because nitrogen is not the element intentionally introduced into the boron-doped MCMB. Its appearance is presumed to be due to the air occluded in the precursor of the petroleum pitch that was packed into the graphite crucible [19].

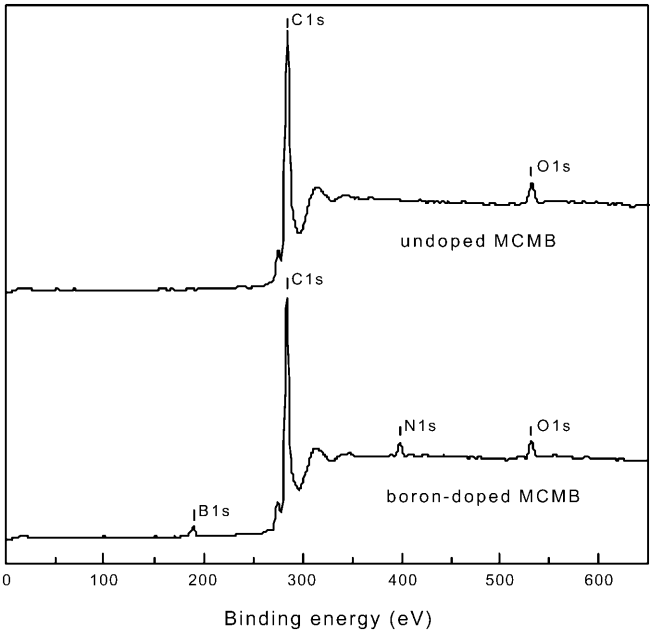

Fig. 1 Wide-scan XPS spectra of undoped and boron-doped MCMB

For sake of clarity, the peaks of C_{1s}, B_{1s}, and N_{1s} were rescanned in high resolution. In Fig. 2 it is shown more clearly that the C_{1s} peak of the boron-doped MCMB is located at slightly lower binding energy compared with the undoped MCMB. The lowering of the binding energy of the C_{1s} peak for boron-doped samples might be due to the lowering of the Fermi level because of the redistributed π-electrons in the graphite layer planes, because the chemical bond formation of the carbon atoms with the electron-deficient boron atoms lowers the density of π-electrons in the graphite layer [20, 21]. Shirasaki et al. [22] have assigned the C_{1s} peak at 283.8 eV to in-plane carbon atoms without boron atoms as first neighbors. Obviously, if more boron is doped, the binding energy of the C_{1s} electron will shift to a lower energy. It is reported that when carbon neighbors with boron atoms pack tightly, the C_{1s} peak is at 282.6 eV; when the B_4C compound is formed, the C_{1s} peak is moved to 281.7 eV [22].

Figure 3 shows the B_{1s} spectrum of the boron-doped sample, consisting of a main peak at 190.3 eV and a shoulder at 186.5 eV. The peak at 190.3 eV may be attributed to B_xC_{1-x} or hexagonal boron nitride. The lower energy component at 186.5 eV corresponds to a boron cluster [22, 23].

Figure 4 illustrates that the N_{1s} peak of the boron-doped sample is constituted with two peaks. The main peak is located at 398.0 eV, which can be assigned the B_3N structure [24, 25], but assignment of the shoulder at 398.6 eV is in abeyance. Gaussian multi-peak fitting indicates that the N_{1s} peak of the boron-doped sample is formed by the overlapping of the main peak at 398.0 eV with a hypo-peak at 398.8 eV, which can be assigned to N-C sp^3 bonding of C_3N_4-like local structure (C-N σ bonds) [26, 27]. It implies that the shoulder peak at

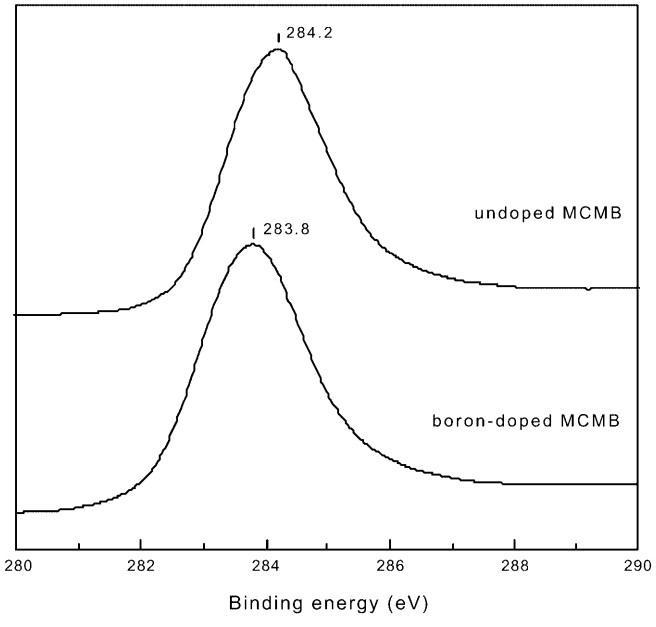

Fig. 2 XPS C_{1s} spectra of undoped and boron-doped MCMB

398.0 eV may be attributed to some boron-substituted carbon nitride structures because boron substitution can shift the bonding energy to a lower direction.

Boron is stabilizing nitrogen in a hexagonal carbon layer, which is why the N_{1s} peak is observed only in the boron-doped sample, as illustrated in Fig. 4 and Fig. 1. Konno et al. [19] have pointed out that when B and N atoms are present together in the hexagonal carbon structure, the most stable energy is the formation of a B-N bond. Thus, referring to the main-peak position of the B_{1s} and N_{1s} peaks in the XPS spectra, it can be speculated that the impurity nitrogen in the boron-doped sample exists mainly in the form of boron nitride clusters. Nitrogen's incorporation will have a certain influence on the structure and properties of boron-doped MCMBs. Its reported incorporation in the boron-doped samples raises the strain in the carbon layers and depresses the development of the graphitic structure. However, contrary to the expectation from its atomic number, it increases the concentration of positive holes in carbon just like boron does [28].

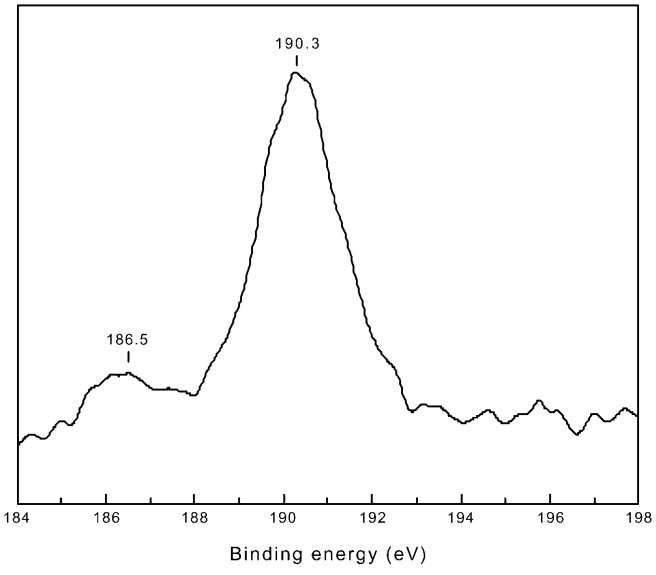

Fig. 3 XPS B_{1s} spectra of boron-doped MCMB

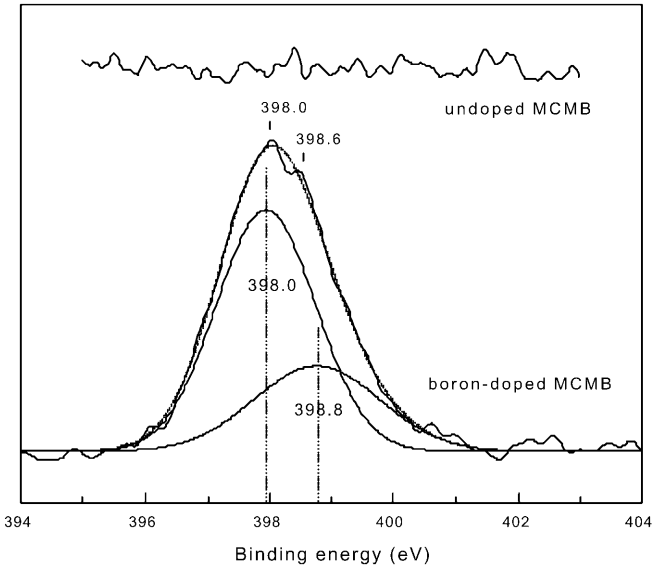

Fig. 4 XPS N_{1s} spectra of undoped and boron-doped MCMB

Morphology change of the materials

Field-emission SEM observations revealed that the boron-doped MCMBs are shaped quite differently from the undoped ones. It can be seen from Fig. 5 that after boron doping the spherical shape of the undoped MCMBs was changed into an irregular and unconsolidated fragmentary graphite-like form. The reason can be traced back to the nucleation and graphitization of the doped boron, which have been discussed above. It can be expected that this morphology transformation caused by boron doping will tamper with the anodic performance of the MCMBs because it obliterates the two

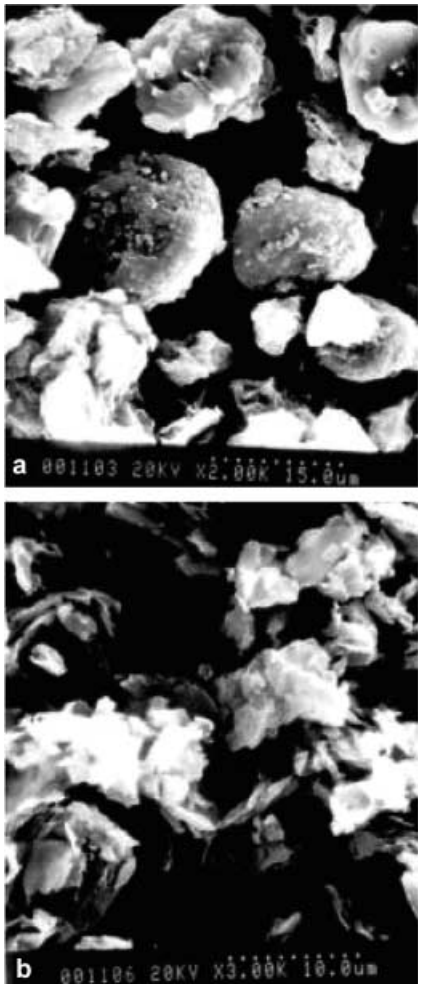

Fig. 5 FE-SEM images of **a** undoped MCMB and **b** boron-doped MCMB

characteristics of the undoped MCMB anode, i.e. the spherical structure and the low surface area.

XRD of the materials

The XRD patterns of the boron-doped and undoped MCMBs are shown in Fig. 6. It is worthwhile to note that the (101), (004), (103), (112), and (006) peaks of carbon in the boron-doped MCMBs are sharper than the corresponding peaks of the undoped MCMBs. Further calculation indicates that, after boron doping, the interlamellar spacing L_c and L_a was increased from 109.52 to 128.84 Å, and from 85.78 to 136.92 Å, respectively. These results imply that the graphitization was improved by boron doping.

In Fig. 6b, the peaks of boron carbide and carbon nitride detected in the boron-doped MCMB accords with the XPS results and SEM observations very well.

Table 1 shows that after boron doping the identity distances (d values) of the hkl plane are decreased when $h=0$ and $k=0$, but increased in other cases. This means that boron doping shortens the distance between graphene planes and elongates the side length of the regular hexagon in the graphene layer. This result suggests that the B-C bond has a longer length than the C-C bond. In fact, molecular simulation work done by Endo et al. [8] gives the lengths of the B-C bonds and C-C bonds in a graphene layer as 1.48 and 1.41 Å, respectively.

Raman spectra of the materials

In Fig. 7, the boron-doped MCMB shows a large increase in the intensity of the D and D′ bands compared to that of the undoped material. For the boron-doped MCMBs the positions of the D and G bands are

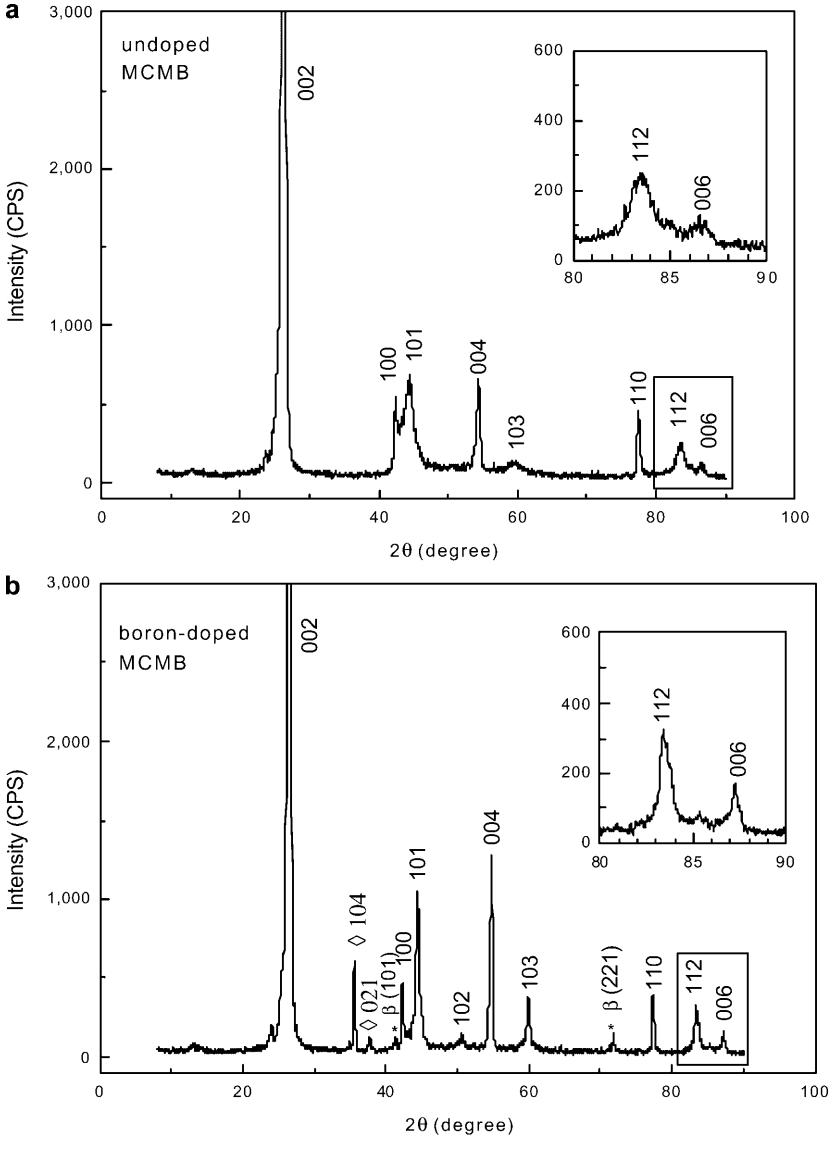

Fig. 6 XRD patterns of **a** undoped MCMB and **b** boron-doped MCMB (*diamonds*: B_xC_{1-x}; *asterisks*: β-C_3N_4)

Table 1 Comparison of the d values calculated from the six strongest peaks of carbon in the XRD patterns of the undoped and boron-doped MCMB by the Bragg equation $n\lambda = 2d\sin\theta$ (in Å)

Peaks	002	100	101	004	110	112
Undoped	3.381	2.129	2.038	1.687	1.231	1.157
Boron-doped	3.353	2.135	2.037	1.675	1.233	1.158
Variation after doping[a]	–	+	+	–	+	+

[a]Decrease (–) and increase (+) of d value after boron doping

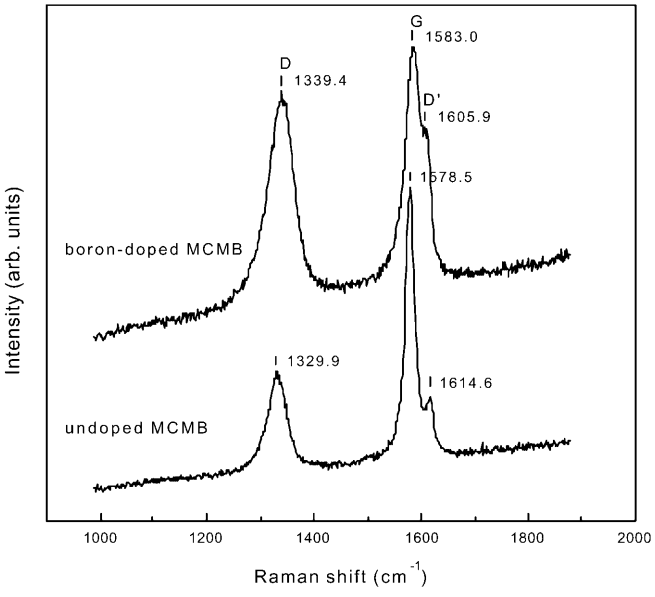

Fig. 7 Raman spectra of undoped and boron-doped MCMB

upshifted. The additional D′ band has a similar origin as the disorder-induced D band because they exhibit similar behavior. Generally, the D band arises from scattering of zone-boundary phonons, which are associated with finite crystallite size effects and/or structural defects, and the D′ band is due predominantly to midzone phonons which have energies corresponding to the peaks in the density of the phonon modes [3, 29]. They are not omnipresent in graphitic materials and become Raman active in our research mainly because of the crystallite size and boron doping.

The G band is relative to the E_{2g} species of hexagonal graphite's infinite single crystal and so is always present in all graphite samples [29]. Its intensity can indicate the degree of graphitization and the orientational alignment of the graphitic planes, but more practically the relative intensity (R value) between the D band and G band varies inversely with the crystallite size (L_a value). The obvious increase of the R value indicates that boron doping decreased the crystallite size, L_a, in the thin surface layer of the sample. The variation of L_a is inconsistent with the results of the XRD pattern. Therefore, it is not appropriate to calculate the crystallite size from the R value for the boron-doped sample. As for the boron-doped MCMBs, the increase of the intensity of the D band corresponds with an increase in the amount of "unorganized carbon" and vacancy formation in the graphite planes [29, 30, 31, 32, 33].

The shift in spectral positions of the D and G bands toward higher wavenumbers in the boron-doped MCMBs is believed to be caused by the different size and type of the near-neighbor bonds from the undoped material, reflecting low local symmetry around the substituent boron atoms [3].

Discharge/charge behavior of the materials

Figure 8 illustrates the discharge/charge curves of both boron-doped and undoped samples. It is obvious that the boron-doped sample carries through the charge and discharge process at a higher potential and finally yields a larger discharge capacity but less charge capacity than the undoped material. However, both samples show charge capacities much less than their corresponding discharge capacities at the first two cycles. This phenomenon may be related to the formation of a solid electrolyte interface (SEI) layer. As we know, in the present research the discharge curves are corresponding to an intercalation process and the charge curves to a deintercalation process because the working electrode is positive to the counter electrode of lithium metal. During the initial discharges the electrolyte decomposition occurs on the surface of the carbon, which leads to the formation of SEIs. This decomposition consumes lithium, so partial intercalated lithium cannot be released during charging and leads to irreversible losses during the initial cycles. Boron doping facilitates the formation of SEIs because it produces irregular and unconsolidated morphology. In Fig. 8, the irreversible capacities (discharge capacity minus charge capacity) of a boron-doped sample at first and second cycle are 156.2 and 69.2 mA h/g respectively, much higher than that of the undoped material (68.0 mA h/g for the first cycle and 1.8 mA h/g for the second cycle). Normally, when the SEI is forming, there is a potential plateau or shoulder clearly visible at 0.7–0.8 V vs. Li/Li^+ on the discharge curve, as shown in Fig. 8a. For the boron-doped samples there is an additional potential shoulder probably occurring at 1.3–1.4 V, because of the strengthened chemical bond between the intercalated lithium and the boron-substituted carbon. As a result, the potential is increased relative to the undoped sample [9, 17, 18]. However, radically, the higher potential of the boron-doped sample can be ascribed to the electron deficiency of the boron substituent.

The boron-doped MCMBs show lower charge capacities compared to the undoped MCMBs. This phenomenon is attributed to the development of the aggregated and recrystallized boron carbide and/or boron nitride [9, 17, 18]. The heterogeneous structure of the boron carbide and/or boron nitride changes the graphite

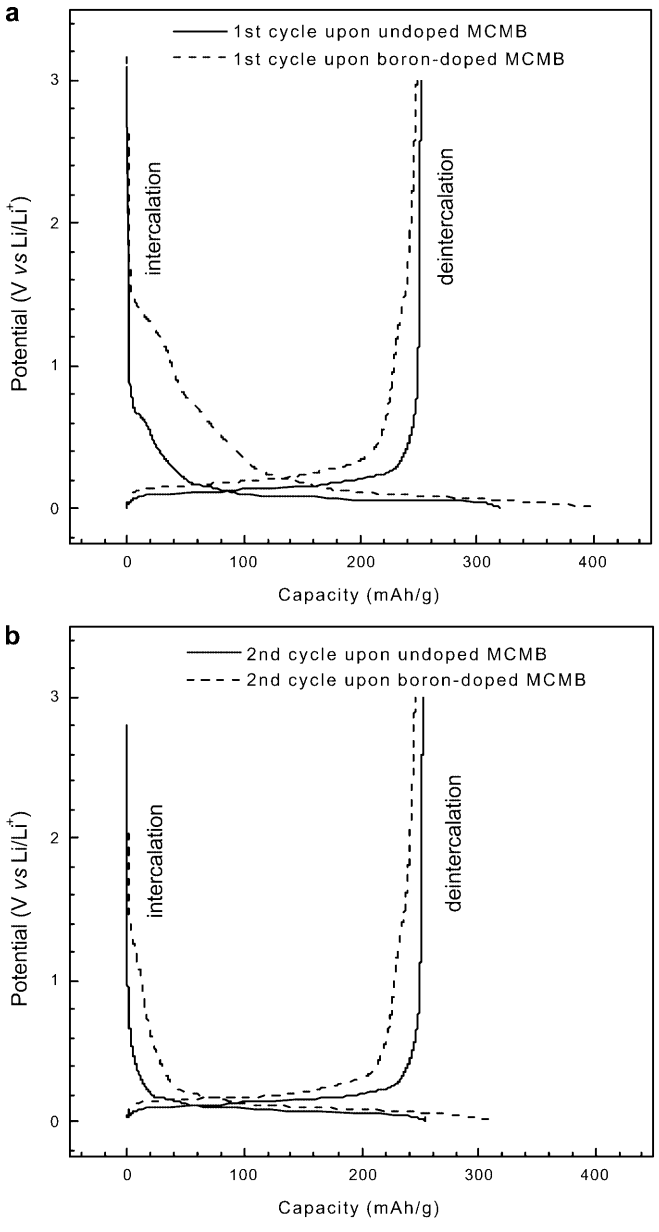

Fig. 8 Discharge/charge curves for undoped and boron-doped MCMB at **a** the first cycle and **b** the second cycle

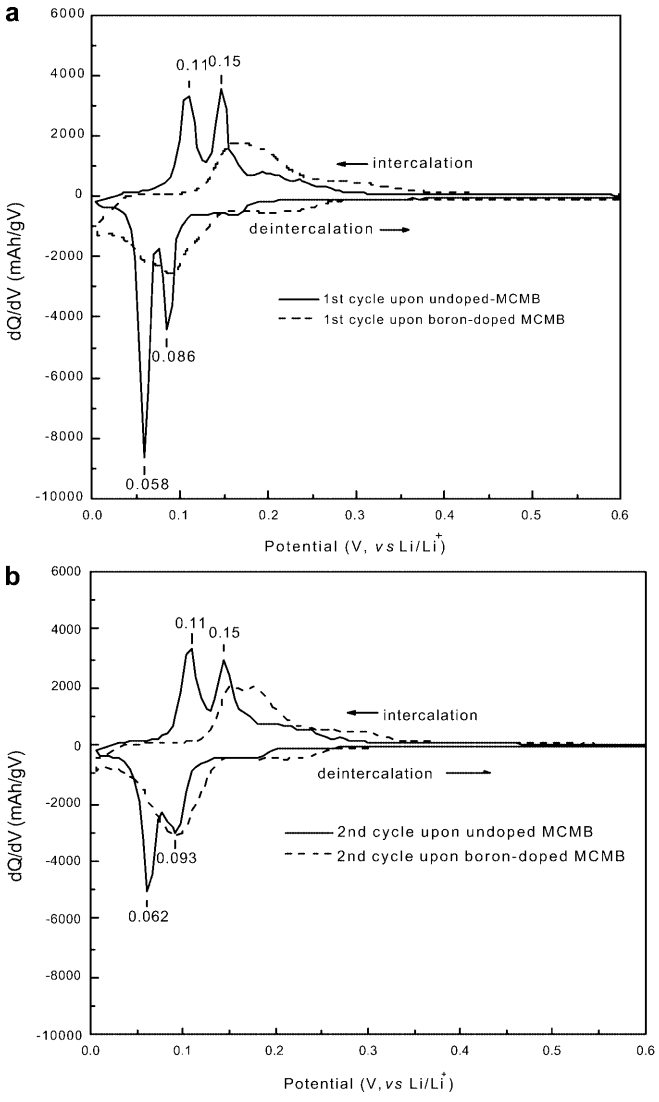

Fig. 9 The differential capacity of **a** the first cycle and **b** the second cycle versus voltage for undoped and boron-doped MCMB

structure morphology of the MCMBs. Additionally, boron carbide and/or boron nitride were also considered to be the cause of the lower capacity of the boron-doped MCMBs, because they are not an active mass for lithium intercalation/deintercalation.

In order to clearly show the different stages of lithium intercalation and deintercalation, differential capacitance (dQ/dV) plots of the first two discharge/charge cycles are drawn in Fig. 9, on which the voltage plateau or shoulder in cycling was transformed into a peak. In the undoped MCMBs, two peaks were observed at 0.11 and 0.15 V in the intercalation process. Correspondingly, only one broad peak around at 0.16 V for the first cycle and two peaks for the second cycle can be seen in the boron-doped sample. It is suggested that the peaks in the differential capacitance plots are occurring when the intercalation electrodes exist as mixtures of coexisting phases. Usually, lithium intercalation into graphite produces four stages, i.e. pure graphite, stage 3, stage 2, stage 1. As for the undoped MCMB, the observed two peaks during the intercalation process, from low potential to high, can be identified as mixtures of pure graphite/stage 3 and stage 3/stage 2, respectively. The absence of the peak at low potential for the boron-doped sample means that there are no pure graphite/stage 3 coexisting phases, showing that boron doping increases the amount of "unorganized carbon" in the graphite structure. It has been suggested that in well-ordered graphite the peaks in the differential capacity curve become sharp with large peak separations due to well-defined phase transitions corresponding to the various stages of the lithium intercalation process [34].

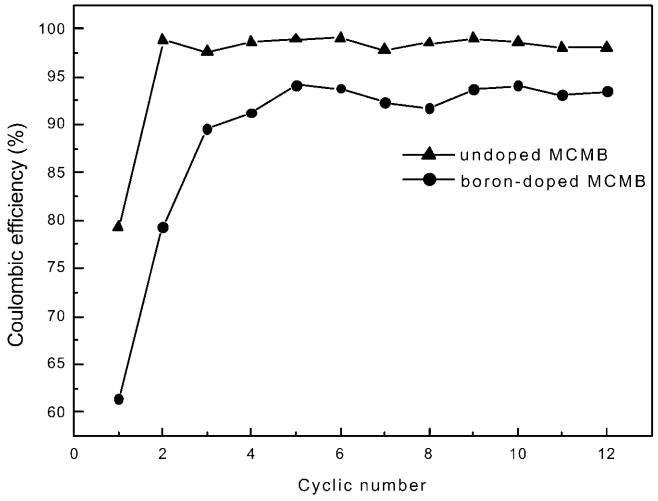

Fig. 10 The coulombic efficiency versus cycle number of undoped and boron-doped MCMB

Coulombic efficiency versus cycle number for the two samples are shown in Fig. 10. The boron-doped MCMB shows worse efficiency than the undoped sample. The phenomenon may be attributed to the amount of "unorganized carbon" and the undesirable morphology of the boron-doped MCMB.

Conclusions

Because of the electron deficiency of boron, boron-doping into MCMBs lowers the density of π-electrons in the graphite layer and the binding energy of carbon. Applying this electronic effect to the crystal structure means that boron doping shortens the identity distance of the graphitic layer and increases the side length of the graphene honeycomb in the *a-b* basal plane. Besides substitution for carbon, boron can combine with carbon to form boron carbide and trap impurity nitrogen as boron nitride or boron-substituted carbon nitride, which were detected by XPS and XRD.

To the morphologies of MCMB powder, boron doping is negative. SEM observations showed that the boron-doped MCMBs have an irregular and unconsolidated structure, quite different from the spherical shape of the undoped material. XRD and Raman spectra analyses indicated that boron doping improves the graphitization, but increases the amount of "unorganized carbon" and induces vacancy formation in the graphite planes.

Aroused from the electrophilic reactivity of substituent boron and the undesirable morphology, the boron-doped MCMBs exhibit higher potential and larger irreversible capacity loss in electrochemical cycle testing experiments. These two features will worsen the electrochemical performance of the boron-doped MCMBs, as the relative higher intercalation potential decreases the working battery voltage when a boron-doped MCMB anode is conjugated with a transition metal oxide cathode, and the larger irreversible capacity reduces the battery's discharge capacity by consuming large amounts of lithium initially stored in the cathode. By these results, we suggest the key to boron doping for better electrochemical performance is morphology control of the doped materials and the content of the doped element.

Acknowledgements The authors acknowledge financial support from the Natural Science Foundation of Fujian Province (no. E0010002).

References

1. Endo M, Kim C, Karaki T, Nishimura Y, Matthews MJ, Brown SDM, Dresselhaus MS (1999) Carbon 37:561
2. Chang Y-C, Sohn H-J, Ku C-H, Wang Y-G, Korai Y, Mochida I (1999) Carbon 37:1285
3. Hagio T, Nakamizo M, Kobayashi K (1989) Carbon 27:259
4. Lowell CE (1967) J Am Ceram Soc 50:142
5. Tatsumi K, Zaghib K, Sawada Y, Abe H, Ohsaki T (1995) J Electrochem Soc 142:1090
6. Way BM, Dahn JR (1994) J Electrochem Soc 141:907
7. Nakajima T, Koh K, Takashima M (1998) Electrochim Acta 43:883
8. Endo M, Kim C, Karaki T, Tamaki T, Nishimura Y, Matthews MJ, Brown SDM, Dresselhaus MS (1998) Phys Rev B 58:8991
9. Endo M, Kim C, Nishimura K, Fujino T, Miyashita K (2000) Carbon 38:183
10. Fujimoto H, Mabuchi A, Tokumitsu K, Kasuh T, Akuzawa N (1994) Carbon 32:193
11. Tasumi K, Iwashita N, Sakaebe H, Shioyama H, Higuchi S, Mabuchi A, Fujimoto H (1995) J Electrochem Soc 142: 716
12. Inaba M, Yoshida H, Ogumi Z (1996) J Electrochem Soc 143:2572
13. Mabuchi A, Tokumitsu K, Fujimoto H, Kasuh T (1995) J Electrochem Soc 142:1041
14. Alcántara R, Fernández Madrigal FJ, Lavela P, Tirado JL, Jiménez Mateos JM, Gómez de Salazar C, Stoyanova R, Zhecheva E (2000) Carbon 38:1031
15. Mabuchi A, Fujimoto H, Tokumitsu K, Kasuh T (1995) J Electrochem Soc 142:3049
16. Tasumi K, Aki T, Imamura T, Zaghib K, Iwashita N, Higuchi S, Sawada Y (1996) J Electrochem Soc 143:1923
17. Kim C, Fujino T, Miyashita K, Hayashi T, Endo M, Dresselhaus MS (2000) J Electrochem Soc 147:1257
18. Kim C, Fujino T, Hayashi T, Endo M, Dresselhaus MS (2000) J Electrochem Soc 147:1265
19. Konno H, Nakahashi T, Inagaki M, Sogabe T (1999) Carbon 37:471
20. Henning G (1965) J Chem Phys 42:1167
21. Jones LE, Thrower PA (1991) Carbon 29:251
22. Shirasaki T, Derre A, Menetrier M, Tressaud A, Flandrois S (2000) Carbon 38:1461
23. Koh M, Nakajima T (1998) Carbon 36:913
24. Kaner RB, Kouvetakis J, Warble CE, Sattler ML, Bartlett N (1987) Mater Res Bull 22:399
25. Kawaguchi M, Kawashima T, Nakajima T (1993) Denki Kagaku 61:1403
26. Boyd KJ, Marton D, Todorov SS, Al-Bayati AH, Kulik J, Zuhr RA, Rabalais JW (1997) J Vac Sci Technol A 12: 322
27. Wang EG (1997) Prog Mater Sci 41:241
28. Inagaki M, Tachikawa H, Nakahashi T, Konno H, Hishiyama Y (1998) Carbon 36:1021

29. Chieu TC, Dresselhaus MS, Endo M (1982) Phys Rev B 26:5867
30. Endo M, Kim C, Karaki T, Tasai T, Nishimura Y, Matthews MJ, Brown SDM, Dresselhaus MS, Tamamki T, Nishimura Y (1998) Carbon 36:1633
31. Tuinstra F, Koenig J (1970) J Chem Phys 53:1126
32. Katagiri G, Takeda N (1996) International conference on coal and organic petrology, vol 11. Fukuoka, Japan, pp 14–16
33. Nishimura K, Kim YA, Matushita T, Endo N, Dresselhaus MS (2000) J Mater Res 15:1213
34. Derosa PA, Balbuena PB (1999) J Electrochem Soc 146: 3630